# Causes of ice age intensification across the Mid-Pleistocene Transition

Thomas B. Chalk[a,b,1,2], Mathis P. Hain[a,1,2], Gavin L. Foster[a], Eelco J. Rohling[a,c], Philip F. Sexton[d], Marcus P. S. Badger[d,e], Soraya G. Cherry[a], Adam P. Hasenfratz[f], Gerald H. Haug[g], Samuel L. Jaccard[h,i], Alfredo Martínez-García[g], Heiko Pälike[a,j], Richard D. Pancost[e], and Paul A. Wilson[a]

[a]Ocean and Earth Science, University of Southampton, National Oceanography Centre Southampton, Southampton SO14 3ZH, United Kingdom; [b]Department of Physical Oceanography, Woods Hole Oceanographic Institution, Woods Hole, MA 02543; [c]Research School of Earth Sciences, The Australian National University, Canberra 2601, Australia; [d]School of Environment, Earth and Ecosystem Sciences, The Open University, Milton Keynes MK7 6AA, United Kingdom; [e]Organic Geochemistry Unit, School of Chemistry, The Cabot Institute, University of Bristol, Bristol BS8 1TS, United Kingdom; [f]Geologisches Institut, Eidgenössische Technische Hochschule Zürich, 8092 Zürich, Switzerland; [g]Max Planck Institut für Chemie, 55128 Mainz, Germany; [h]Institute of Geological Sciences, University of Bern, 3012 Bern, Switzerland; [i]Oeschger Center for Climate Change Research, University of Bern, 3012 Bern, Switzerland; and [j]Center for Marine Environmental Sciences (MARUM), University of Bremen, 28359 Bremen, Germany

Edited by Maureen E. Raymo, Lamont–Doherty Earth Observatory of Columbia University, Palisades, NY, and approved September 7, 2017 (received for review February 9, 2017)

**During the Mid-Pleistocene Transition (MPT; 1,200–800 kya), Earth's orbitally paced ice age cycles intensified, lengthened from ∼40,000 (∼40 ky) to ∼100 ky, and became distinctly asymmetrical. Testing hypotheses that implicate changing atmospheric $CO_2$ levels as a driver of the MPT has proven difficult with available observations. Here, we use orbitally resolved, boron isotope $CO_2$ data to show that the glacial to interglacial $CO_2$ difference increased from ∼43 to ∼75 μatm across the MPT, mainly because of lower glacial $CO_2$ levels. Through carbon cycle modeling, we attribute this decline primarily to the initiation of substantive dust-borne iron fertilization of the Southern Ocean during peak glacial stages. We also observe a twofold steepening of the relationship between sea level and $CO_2$-related climate forcing that is suggestive of a change in the dynamics that govern ice sheet stability, such as that expected from the removal of subglacial regolith or interhemispheric ice sheet phase-locking. We argue that neither ice sheet dynamics nor $CO_2$ change in isolation can explain the MPT. Instead, we infer that the MPT was initiated by a change in ice sheet dynamics and that longer and deeper post-MPT ice ages were sustained by carbon cycle feedbacks related to dust fertilization of the Southern Ocean as a consequence of larger ice sheets.**

boron isotopes | MPT | geochemistry | carbon dioxide | paleoclimate

The Mid-Pleistocene Transition (MPT) marks a major shift in the response of Earth's climate system to orbital forcing. During the Early Pleistocene, glacial–interglacial (G-IG) climate cycles were paced by ∼40,000 y (40 ky) obliquity cycles, whereas G-IG cycles after the MPT gradually intensified over multiple obliquity cycles (i.e., 80- to 120-ky periodicity) (1, 2) and acquired a distinctively asymmetric character with gradual glacial growth and abrupt glacial terminations that were paced by a combination of obliquity and precession (1). These changes gave rise to longer, colder, and dustier Late Pleistocene ice ages with larger continental ice sheets and lower global sea level (SL) (3–5) (Fig. 1). The MPT occurred in the absence of any significant change in the pacing or amplitude of orbital forcing, indicating that it arose from an internal change in the response of the climate system rather than a change in external forcing (1, 6, 7).

Proposed explanations for the MPT fall into two primary groups: those that invoke a change in ice sheet dynamics and those that call on some subtle change in the climate system's global energy budget. Two prominent hypotheses posit that either removal of the subglacial regolith beginning at about 1,200 ky (8, 9) or phase-locking of Northern and Southern Hemisphere ice sheets at about 1,000 ky (10) gave rise to deeper and ultimately longer G-IG climate cycles by allowing for a greater buildup of ice independent of a change in $CO_2$ radiative climate forcing (scenario 1 in Fig. 2). Alternatively, it has been argued that an underlying change in the global carbon cycle could have triggered the MPT through a decline in $\Delta R_{CO2}$ [i.e., the radiative climate forcing exerted by $CO_2$ decline (11–13) (scenario 2 in Fig. 2)]. The continuous 800-ky-long ice core record of atmospheric $CO_2$ (i.e., compiled by ref. 14) is well-correlated to and shares spectral power with orbital-scale changes in temperature, ice volume, SL, and the oxygen isotopic composition of benthic foraminifera (Figs. 1 and 3). State of the art coupled climate–ice sheet models can simulate climate cycles that are longer than single obliquity cycles, provided that mean $CO_2$ concentrations are within certain model-dependent bounds (15, 16) (e.g., 200–260 μatm). These studies suggest that the absolute $CO_2$ level attained during rising obliquity (i.e., during increasing high-latitude Northern Hemisphere summer insolation) may be a critical control that determines whether ice sheets are strictly locked to the ∼40-ky beat of obliquity or survive for longer periods. Recent work has provided some evidence for an overall $CO_2$ decline since the MPT (11, 17), supporting this view. The study by Hönisch et al. (11), in particular, provides

## Significance

Conflicting sets of hypotheses highlight either the role of ice sheets or atmospheric carbon dioxide ($CO_2$) in causing the increase in duration and severity of ice age cycles ∼1 Mya during the Mid-Pleistocene Transition (MPT). We document early MPT $CO_2$ cycles that were smaller than during recent ice age cycles. Using model simulations, we attribute this to post-MPT increase in glacial-stage dustiness and its effect on Southern Ocean productivity. Detailed analysis reveals the importance of $CO_2$ climate forcing as a powerful positive feedback that magnified MPT climate change originally triggered by a change in ice sheet dynamics. These findings offer insights into the close coupling of climate, oceans, and ice sheets within the Earth System.

Author contributions: T.B.C., M.P.H., G.L.F., E.J.R., A.P.H., G.H.H., S.L.J., A.M.-G., R.D.P., and P.A.W. designed research; T.B.C., M.P.H., M.P.S.B., and S.G.C. performed research; T.B.C., M.P.H., G.L.F., E.J.R., P.F.S., S.G.C., H.P., and P.A.W. analyzed data; and T.B.C. and M.P.H. wrote the paper.

The authors declare no conflict of interest.

This article is a PNAS Direct Submission.

This open access article is distributed under Creative Commons Attribution-NonCommercial-NoDerivatives License 4.0 (CC BY-NC-ND).

Data deposition: The data reported in this paper have been deposited in the Pangaea database (https://doi.pangaea.de/10.1594/PANGAEA.882551).

[1]T.B.C. and M.P.H. contributed equally to this work.

[2]To whom correspondence may be addressed. Email: T.chalk@noc.soton.ac.uk or M.P.Hain@soton.ac.uk.

This article contains supporting information online at www.pnas.org/lookup/suppl/doi:10.1073/pnas.1702143114/-/DCSupplemental.

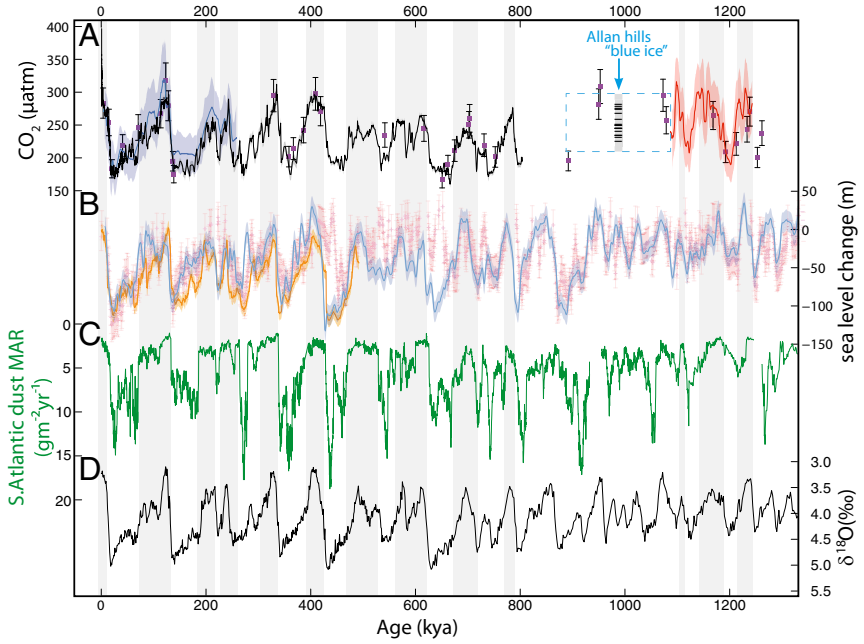


**Fig. 1.** Climate records across the MPT. (*A*) $CO_2$ records are shown as follows: black line, ice core compilation (14); blue, our $\delta^{11}B$-based LP260 data; red, our $\delta^{11}B$-based eMPT data; and purple squares, low-resolution MPT $\delta^{11}B$ record of ref. 11 (all with $2\sigma$ error bars/envelopes). The range of ice core $CO_2$ measurements (17) from stratigraphically disturbed blue ice and their approximate ages are indicated. (*B*) SL records, where orange indicates the Red Sea record (21), dark blue represents Mg/Ca-based deconvolution of deep sea benthic foraminiferal oxygen isotope data (3), and pink shows a record from the Mediterranean Sea (4). (*C*) Dust mass accumulation rate (MAR) in a sub-Antarctic site ODP 1090 on the southern flank of the Agulhas Ridge (24). (*D*) LR04 benthic foraminiferal oxygen isotope stack (26). Warm intervals are highlighted by gray bars.

evidence that $CO_2$ decline was most pronounced during glacial stages. Here, we build on that work with the aim to resolve the coupling of $CO_2$ and climate on orbital timescales to address major unanswered questions regarding the role of $CO_2$ change in the MPT.

To better quantify the role of $CO_2$ during the MPT, we present two orbitally resolved, boron isotope-based $CO_2$ records generated using the calcite tests of surface-dwelling planktonic foraminifera from Ocean Drilling Program (ODP) Site 999 in the Caribbean (Fig. 3 and Figs. S1 and S2). Boron isotopes ($\delta^{11}B$) in foraminifera have proven to be a reliable indicator of past ocean pH (18, 19) and with appropriate assumptions regarding a second carbonate system parameter (*Materials and Methods* and Fig. S3), allow reconstruction of atmospheric $CO_2$ levels. Site 999 likely remained near air–sea $CO_2$ equilibrium through time (20), and this is further supported by agreement of our data (blue and red in Figs. 1*A* and 3) with published low-resolution $\delta^{11}B$-derived $CO_2$ data from ODP Site 668 in the equatorial Atlantic (11) (purple squares in Figs. 1*A* and 3*B*) and with the ice core $CO_2$ compilation (14).

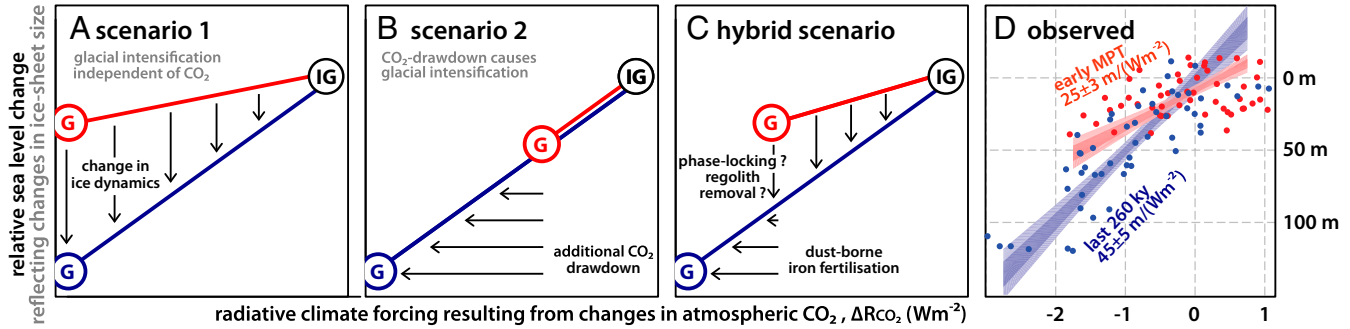


**Fig. 2.** Changing relationship between $CO_2$ climate forcing and ice sheet size. Three scenarios (*A*–*C*) for the MPT intensification of glacial cycles compared with observations (*D*). Reconstructed SL is taken here to reflect continental ice sheet size in relationship to $CO_2$ climate forcing ($\Delta R_{CO2}$) calculated (33) from our orbitally resolved $CO_2$ data. In all panels, red and blue represent conditions during our two sampling intervals before and after the MPT (i.e., eMPT and LP260), respectively. The end member scenarios posit (*A*) a change in ice sheet dynamics, causing ice volume to become more sensitive to unchanged G-IG climate forcing, and (*B*) an unchanged sensitivity of ice sheet size to forcing, with glacial intensification driven by additional $CO_2$ drawdown. Neither one of these two scenarios adequately describes both observed changes of increased ice sheet sensitivity (greater slope) and additional glacial $CO_2$ drawdown (more negative climate forcing). Here, we argue for a hybrid scenario with a change in ice sheet dynamics (possibly caused by regolith removal of ref. 8 or ice sheet phase-locking of ref. 10), allowing ice sheets to grow larger and to trigger a positive ice–dust–$CO_2$ feedback that promotes additional glacial intensification. In *D*, the regression confidence intervals account for uncertainty in both SL and $\Delta R_{CO2}$ (*SI Forcing to SL Relationship*), but to avoid clutter, we only display the regression based on the Mediterranean SL reconstruction (4) and the uncertainty on the slope rather than the individual data points. We refer the reader to *SI Forcing to SL Relationship* and Fig. S7 for other SL records and full treatment of data uncertainties.

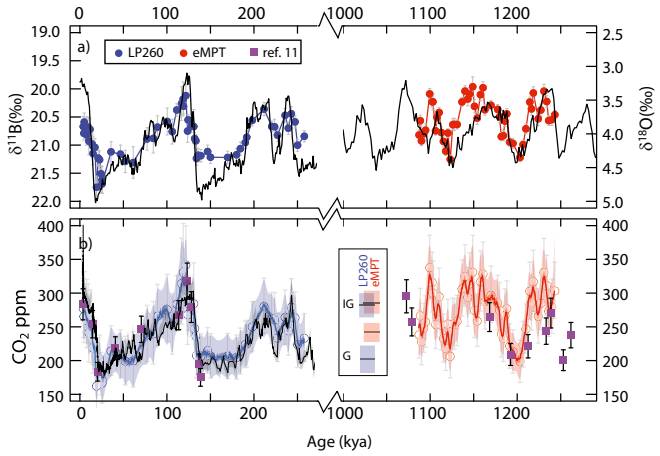


**Fig. 3.** Reconstructed ice age $CO_2$ cycles before and after MPT. (*A*) Boron isotope data from ODP 999 (Fig. S1) shown in blue (LP260) and red (eMPT) along with the LR04 deep sea benthic foraminiferal oxygen isotope stack (black) (26). (*B*) $CO_2$ levels calculated from boron isotopes (same colors as above) compared with ice core (black) (14) and previous low-resolution boron-derived $CO_2$ data (purple) (11). Probabilistic assessments are shown as the colored bands, with the probability maximum shown within a dark band that represents its 95% probability envelope (~±6 ppm) and a lighter band that represents the full 95% envelope of the sampled distribution. As illustrated by *B*, *Inset*, comparison between our (red) eMPT and (blue) LP260 records reveals that glacials on average experienced higher $CO_2$ levels during eMPT than LP260 (eMPT: 241 ± 21 µatm vs. LP260: 203 ± 14 µatm; 2σ), whereas interglacial levels were indistinguishable between the two time slices (eMPT: 284 ± 17 µatm vs. LP260: 277 ± 18 µatm; 2σ).

## Results

Our two datasets span an early portion of the Mid-Pleistocene Transition (eMPT) from 1,080 to 1,250 kya ($n$ = 51) and for validation against the ice core $CO_2$ record, the Pleistocene interval from 0 to 260 kya (LP260; $n$ = 59, including 32 recalculated data points from ref. 18), yielding a similar median sampling interval of ~3.5–4.5 ky for both records. Our LP260 $CO_2$ dataset has a confidence interval of ±20 µatm (2σ) and is offset by a mean of +7 µatm from the ice core $CO_2$ data when accounting for both $CO_2$ and age uncertainties (21) (Fig. 3*B* and *SI Methodology*). Comparison between our two $CO_2$ records reveals that eMPT glacials on average were associated with higher $CO_2$ levels than LP260 glacials (eMPT: 241 ± 21 µatm vs. LP260: 203 ± 14 µatm; 2σ), whereas interglacial levels were indistinguishable (eMPT: 284 ± 17 µatm vs. LP260: 277 ± 18 µatm; 2σ). This analysis uses highest and lowest 25th percentiles of $\delta^{18}O$ values to define "glacial" and "interglacial" subsets of the data, although this pattern is independent of the thresholds that we define (Fig. 4 and Fig. S4). Our analysis reproduces the glacial stage-specific decline in $CO_2$ levels found in ref. 11, leading to similar reconstructed increases in the glacial to interglacial $CO_2$ difference since the MPT (40 ± 47 and 32 ± 35 µatm based on ref. 11 and our data, respectively) (Fig. 4). The higher resolution of these datasets allows this approach to yield useful data about our timespans, despite the relatively large uncertainty on each individual data point. When analyzed in a similar way, recent direct measurements of $CO_2$ from a stratigraphically disturbed section of ~1-My-old "blue ice" (17) offer a fully independent test for the two $\delta^{11}B$-based reconstructions and are consistent with these findings (Fig. 4 and Fig. S4). Thus, all available evidence suggests that the MPT was associated with a transition in the global carbon cycle characterized mainly by enhanced glacial-stage drawdown of $CO_2$.

We evaluate the reconstructed G-IG $CO_2$ change across our study interval with a carbon cycle model inversion of Southern Ocean and Atlantic mechanisms thought to have contributed to the most recent Late Pleistocene G-IG $CO_2$ cycles (22). For this, we force the CYCLOPS carbon cycle model (23) with ODP 1090 sedimentary iron mass accumulation rates (24), ODP 1094 Ba/Fe ratios (25), and ODP 982/U1313 (Fig. S1) benthic $\Delta\delta^{13}C$ variations (26, 27) to represent, respectively, (*i*) sub-Antarctic dust-borne iron fertilization; (*ii*) combined changes in polar Antarctic stratification, nutrient drawdown, and export production; and (*iii*) transitions in the geometry and depth structure of the Atlantic Meridional Overturning Circulation (AMOC) (Fig. S5). These mechanisms and their model sensitivities have been documented elsewhere (23). Here, we invert the model and the forcing to minimize the mismatch between simulated atmospheric $CO_2$ levels and the ice core $CO_2$ record of the last 800 ky (residual rms error of 12.3 µatm) (*SI Carbon Cycle Modeling*) and then, to predict atmospheric $CO_2$ levels back to 1,500 ky (Fig. S5) for comparison with our data.

We find that changes in the periodicity of simulated $CO_2$ levels closely match those in the ice core $CO_2$ record, in the benthic foraminiferal oxygen isotope record, and in our $\delta^{11}B$-based $CO_2$ reconstruction (Fig. S6). Within the relative age uncertainty between the model forcing and our $\delta^{11}B$ record, we find that the model explains more than 60% of the variance observed in our eMPT $CO_2$ reconstruction, in line with model and reconstruction uncertainties. The model inversion does not include any secular change in the silicate weathering cycle (11) (*SI Carbon Cycle Modeling*), so that simulated $CO_2$ change is exclusively related to carbon redistribution within the ocean–atmosphere system and associated $CaCO_3$ compensation dynamics (22, 23).

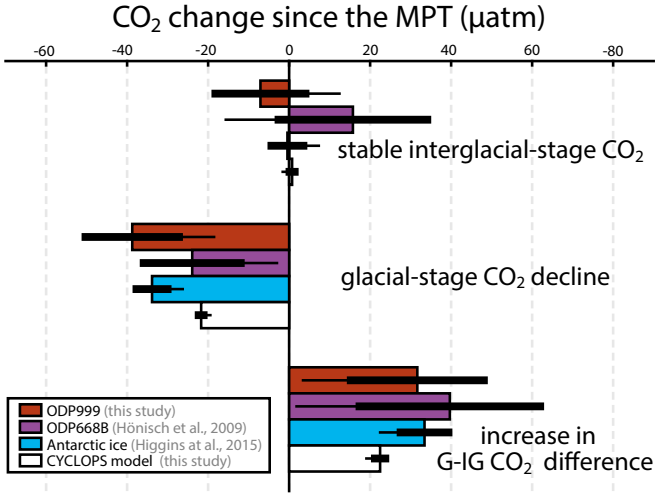


**Fig. 4.** $CO_2$ change since the MPT. Quantified from different datasets: boron isotope data from ODP 999 (this study) and ODP 668 (11), $CO_2$ directly measured on stratigraphically disturbed ~1-My-old blue ice from the Allan Hills (17), and CYCLOPS model inversion (this study). For each dataset, we quantify the change in (*Top*) interglacial and (*Middle*) glacial $CO_2$ level as well as (*Bottom*) the change in the magnitude of interglacial–glacial $CO_2$ cycles. For this analysis, we define glacial and interglacial subsets of the datasets based on a 25% cutoff criterion, subsampling the data with the 25% lowest/highest $\delta^{18}O$ (marine records) or $CO_2$ (ice core; model). As further discussed in *SI Quantification of* $^{G}CO_2$, $^{IG}CO_2$, *and* $^{IG\text{-}G}\Delta CO_2$, the results are robust for a wide range of cutoff values (Fig. S4). Thick black bars denote 1σ uncertainty of the estimated $CO_2$ change, while thin black bars denote the one-sided test of the sign of $CO_2$ change at 95% significance level. We note that the ODP 668 uncertainties do not encompass the underlying alkalinity and seawater boron isotope composition assumptions, which are included in the uncertainty propagation for our ODP 999 data. The Allan Hills ice may not capture the full range of $CO_2$ levels (17).

In good agreement with the $\delta^{11}$B-based $CO_2$ reconstructions and the ice core $CO_2$ measurements, the model inversion yields (*i*) insignificant ($-1 \pm 3$ μatm; $2\sigma$) eMPT to LP260 interglacial $CO_2$ change and (*ii*) a $-22 \pm 5$ μatm ($2\sigma$) eMPT to LP260 decline in glacial-stage $CO_2$ levels (Fig. 4 and Fig. S4). In the model, we can attribute most of the additional glacial $CO_2$ drawdown to MPT intensification of glacial dust-borne iron fertilization of biological productivity and nutrient utilization in the Sub-Antarctic Zone of the Southern Ocean (24, 28–30) (Fig. S5). AMOC shoaling also seems to have become more prevalent after ~1,200 ky but contributes less to simulated $CO_2$ change (23). The model reproduces relatively low reconstructed interglacial $CO_2$ from 400 to 800 ky, because use of ODP 1094 Ba/Fe in the model inversion results in persistent polar Southern Ocean stratification as suggested previously (25). Through our eMPT sample interval, the model reproduces the ~80-ky $CO_2$ periodicity that is evident in our eMPT $\delta^{11}$B data (Fig. S6), mainly because of an ~80-ky periodicity in eMPT polar Antarctic stratification and nutrient cycling recorded in ODP 1094 Ba/Fe (25). While all three forcings (iron fertilization, Atlantic circulation, coupled polar Antarctic changes) contribute to the simulated changes in $CO_2$ periodicities that are highly coherent with the MPT change in rhythm of the climate system, the iron fertilization influence dominates the MPT intensification of ice age $CO_2$ drawdown (Fig. S5).

## Discussion

MPT intensification of glacial-stage $CO_2$ drawdown is consistent with stabilization of continental ice sheets during increasing orbital obliquity by reduced greenhouse gas forcing, thereby helping ice sheets to grow larger and for periods longer than one obliquity cycle (scenario 2 in Fig. 2). However, when we directly compare changes in SL as a measure for ice volume against $CO_2$ climate forcing ($\Delta R_{CO2}$) from our records (Fig. 2*D*), we find that, between eMPT and LP260, ice sheet mass increased progressively more per $CO_2$ lowering, thereby increasing the SL–$\Delta R_{CO2}$ slope in Fig. 2. This suggests an increase in ice sheet sensitivity to $CO_2$ forcing across the MPT, with the caveat that eMPT may not fully capture pre-MPT conditions, although it agrees with the longer-term record of Hönisch et al. (11). This finding is robust, regardless of which SL reconstruction is used (Fig. S7); in all cases, the SL to $\Delta R_{CO2}$ relationships appear to be linear, with increasing slopes from eMPT to LP260. The steepening relationship is also evident when regressing $\delta^{11}$B to $\delta^{18}$O relationships, with both isotope ratios measured on the same sample material (Fig. S8). Using the SL record with the best coverage of both intervals, relative SL from the Mediterranean Sea (4), we estimate $25 \pm 3$ and $45 \pm 5$ m of SL lowering for each 1-$Wm^{-2}$ reduction in radiative forcing during eMPT and LP260, respectively. Such a pronounced increase in sensitivity implicates a change in ice sheet dynamics as predicted by the regolith hypothesis (8, 9) or the establishment of marine-based ice sheet margins in East Antarctica (10) (scenario 1 in Fig. 2).

The observed changes in the SL to $\Delta R_{CO2}$ relationships contain elements of both end member scenarios shown in Fig. 2 *A* and *B*, in which a greater slope is possibly related to changes internal to the ice sheets (scenario 1) and amplified glacial to interglacial $CO_2$ climate forcing is linked (this study) to increased glacial dustiness that causes enhanced Southern Ocean iron fertilization (scenario 2). Therefore, we propose a hybrid scenario (Fig. 2*C*) that incorporates both heightened ice sheet sensitivity to $CO_2$ forcing and dust-driven ocean sequestration of $CO_2$ to represent the observed climate system change across the MPT.

First, we propose that—independent of orbital and $CO_2$ forcing—a process internal to the climate system yielded greater glacial buildup of ice sheets [e.g., regolith removal (8) or ice sheet phase-locking (10)]. Second, we infer that larger ice sheets led to increased glacial atmospheric dustiness (31, 32), either directly through SL lowering or indirectly because of atmospheric cooling, drying, and/or changes in surface winds. This, in turn, induced glacial iron fertilization of the Sub-Antarctic Zone of the Southern Ocean, thereby effecting the 20- to 40-μatm increase in the amplitude of the G-IG $CO_2$ cycles documented here (Fig. 4) (11). In our hybrid scenario, the positive climate–dust–$CO_2$ feedback is required to (*i*) drive additional ice sheet growth and (*ii*) stabilize those ice sheets during the critical orbital phase of rising obliquity, ensuring the survival of ice sheets beyond single obliquity cycles. Therefore, regardless of the mechanism that served as the initial MPT trigger, our findings further illustrate the exquisite coupling that exists in the Earth System between climate change, ice sheet mass, and the polar ocean mechanisms that regulate G-IG $CO_2$ change.

## Materials and Methods

*Globigerinoides ruber* white *sensu stricto* (300–355 μm) were picked from sediments from ODP 999A (Fig. S1), and the age model was constructed by benthic oxygen isotopes from the same samples and X-ray fluorescence scanning data. Samples were measured for boron isotope composition using a Thermo Scientific Neptune multicollector inductively coupled plasma mass spectrometer at the University of Southampton according to methods described elsewhere (18). Analytical uncertainty is given by the external reproducibility of repeat analyses of Japanese Geological Survey Porites coral standard at the University of Southampton and is typically <0.2‰ (at 95% confidence). Metal element–calcium ratios (Mg, B, Al) were analyzed using Thermo Element 2XR inductively coupled plasma mass spectrometer at the University of Southampton. Here, these data are used to assess adequacy of clay removal (Al/Ca < 100 μmol/mol) and to generate down core temperature estimates. $CO_2$ was calculated using a Monte Carlo approach (10,000 replicates) with estimates of salinity and alkalinity using a flat probability spanning a generous range (34–37 psu and 2,100–2,500 μmol/kg, respectively). A normal distribution around proxy data was used for all other input variables (temperature, pH, $\delta^{11}B_{sw}$, $\delta^{11}B_{foram}$) (*SI Methodology* has full details). The $CO_2$ record was then probabilistically assessed using a Monte Carlo approach that considers uncertainties in both age and $CO_2$ values and that preserves the stratigraphy of the record, which minimizes age uncertainty in a relative sense between samples (shown as an envelope in Figs. 1 and 3). Each of 2,000 Monte Carlo iterations involved independent random resampling of each sample within its *x* and *y* uncertainty distributions. The stratigraphic constraint prevents age reversals in this resampling procedure. Linear interpolation was performed between resampled points, and the distribution of values thus generated was analyzed per time step for the modal value and its 95% probability interval as well as the 95% probability envelope of data in the sampled distribution (using the 2.5th and 97.5th percentiles). Because uncertainties in both *x* and *y* directions are considered, the record of probability maxima (modes) gives a smoothed representation of the record, with quantified uncertainties (*SI Forcing to SL Relationship*).

Inverse carbon cycle modeling was carried out using the CYCLOPS model (23), with the forward model forcing derived from pertinent paleoceanographic records (25–27) and the forcing scaling parameters inverted to minimize model misfit with respect to the ice core $CO_2$ record of the last 800 ky. Significant linear correlation with and matching spectral content to our boron isotope-based $CO_2$ data confirm the skill of the model inversion (Fig. S6). Detailed statistical analysis is carried out to identify and quantify changes in absolute glacial and interglacial $CO_2$ as well as the G-IG $CO_2$ range from the model inversion results, our high-resolution $CO_2$ data, and some previous datasets (11, 17) that are not well dated or lack the required temporal resolution for comparison in the time and/or frequency domains. This analysis is based on estimation of the population means of cumulative probability density of glacial and interglacial subsamples, which were selected based on either available benthic foraminiferal $\delta^{18}$O or $CO_2$ rank (Fig. 4). Factorial analysis of the validated model allows for the mechanistic attribution to sub-Antarctic iron fertilization of glacial stage-specific $CO_2$ reduction associated with the MPT interval (Fig. S5, *Bottom*), which is the pattern that we identified as common between model and all three empirical datasets. More detailed descriptions of inverse modeling and model/data cross-validation and statistical quantification of $CO_2$ change can be found in *SI Carbon Cycle Modeling* and *SI Quantification of* $^{G}CO_2$, $^{IG}CO_2$, *and* $^{IG\text{-}G}\Delta CO_2$, respectively.

**ACKNOWLEDGMENTS.** We thank J. A. Milton, M. Cooper, A. Michalik, M. Spencer, and members of the "boron-team" at the University of Southampton

for analytical help; the Integrated Ocean Drilling Program (IODP) Gulf Coast core repository for sample provision; and R. James, E. McClymont, R. Greenop, W. Kordesch, J. Higgins, and D. Sigman for discussion. This work used samples provided by the International Ocean Discovery Program, which is sponsored by the US National Science Foundation and participating countries under the management of the Joint Oceanographic Institutions. Research was supported by National Environmental Research Council (NERC) Studentship NE/I528626/1 (to T.B.C.); NERC Grant NE/P011381/1 (to T.B.C., M.P.H., G.L.F., E.J.R., and P.A.W.); NERC Fellowships NE/K00901X/1 (to M.P.H.), NE/I006346/1 (to G.L.F. and R.D.P), and NE/H006273/1 (to R.D.P.); Royal Society Wolfson Awards (to G.L.F. and P.A.W.); Australian Research Council Laureate Fellowship FL1201000050 (to E.J.R.); Swiss National Science Foundation Grant PP00P2-144811 (to S.L.J.); ETH Research Grant ETH-04 11-1 (to S.L.J.); European Research Council Consolidator Grant (ERC CoG) Grant 617462 (to H.P.); and NERC UK IODP Grant NE/F00141X/1 (to P.A.W.).

1. Huybers P (2011) Combined obliquity and precession pacing of late Pleistocene deglaciations. *Nature* 480:229–232.
2. Clark PU, et al. (2006) The middle Pleistocene transition: Characteristics, mechanisms, and implications for long-term changes in atmospheric $pCO_2$. *Quat Sci Rev* 25: 3150–3184.
3. Elderfield H, et al. (2012) Evolution of ocean temperature and ice volume through the mid-Pleistocene climate transition. *Science* 337:704–709.
4. Rohling EJ, et al. (2014) Sea-level and deep-sea-temperature variability over the past 5.3 million years. *Nature* 508:477–482.
5. McClymont EL, Sosdian SM, Rosell-Melé A, Rosenthal Y (2013) Pleistocene sea-surface temperature evolution: Early cooling, delayed glacial intensification, and implications for the mid-Pleistocene climate transition. *Earth Sci Rev* 123:173–193.
6. Imbrie J, et al. (1993) On the structure and origin of major glaciation cycles. 2. The 100,000-year cycle. *Paleoceanography* 8:699–735.
7. Pisias NG, Moore T (1981) The evolution of Pleistocene climate: A time series approach. *Earth Planet Sci Lett* 52:450–458.
8. Clark PU, Pollard D (1998) Origin of the middle Pleistocene transition by ice sheet erosion of regolith. *Paleoceanography* 13:1–9.
9. Snyder CW (2016) Evolution of global temperature over the past two million years. *Nature* 538:226–228.
10. Raymo ME, Huybers P (2008) Unlocking the mysteries of the ice ages. *Nature* 451: 284–285.
11. Hönisch B, Hemming NG, Archer D, Siddall M, McManus JF (2009) Atmospheric carbon dioxide concentration across the mid-Pleistocene transition. *Science* 324:1551–1554.
12. Raymo ME, Ruddiman WF, Froelich PN (1988) Influence of late Cenozoic mountain building on ocean geochemical cycles. *Geology* 16:649–653.
13. Berger A, Li X, Loutre M (1999) Modelling northern hemisphere ice volume over the last 3 Ma. *Quat Sci Rev* 18:1–11.
14. Bereiter B, et al. (2015) Revision of the EPICA Dome C $CO_2$ record from 800 to 600 kyr before present. *Geophys Res Lett* 42:542–549.
15. Abe-Ouchi A, et al. (2013) Insolation-driven 100,000-year glacial cycles and hysteresis of ice-sheet volume. *Nature* 500:190–193.
16. Ganopolski A, Calov R (2011) The role of orbital forcing, carbon dioxide and regolith in 100 kyr glacial cycles. *Clim Past* 7:1415–1425.
17. Higgins JA, et al. (2015) Atmospheric composition 1 million years ago from blue ice in the Allan Hills, Antarctica. *Proc Natl Acad Sci USA* 112:6887–6891.
18. Foster GL (2008) Seawater pH, $pCO_2$ and $CO_3^{2-}$ variations in the Caribbean Sea over the last 130 kyr: A boron isotope and B/Ca study of planktic foraminifera. *Earth Planet Sci Lett* 271:254–266.
19. Hönisch B, Hemming NG, Loose B (2007) Comment on "A critical evaluation of the boron isotope-pH proxy: The accuracy of ancient ocean pH estimates" by M. Pagani, D. Lemarchand, A. Spivack and J. Gaillardet. *Geochim Cosmochim Acta* 71:1636–1641.
20. Martínez-Botí MA, et al. (2015) Plio-Pleistocene climate sensitivity evaluated using high-resolution $CO_2$ records. *Nature* 518:49–54.
21. Grant KM, et al. (2014) Sea-level variability over five glacial cycles. *Nat Commun* 5:5076.
22. Sigman DM, Hain MP, Haug GH (2010) The polar ocean and glacial cycles in atmospheric $CO_2$ concentration. *Nature* 466:47–55.
23. Hain MP, Sigman DM, Haug GH (2010) Carbon dioxide effects of Antarctic stratification, North Atlantic Intermediate Water formation, and subantarctic nutrient drawdown during the last ice age: Diagnosis and synthesis in a geochemical box model. *Global Biogeochem Cycles* 24:GB4023.
24. Martínez-Garcia A, et al. (2011) Southern Ocean dust-climate coupling over the past four million years. *Nature* 476:312–315.
25. Jaccard SL, et al. (2013) Two modes of change in Southern Ocean productivity over the past million years. *Science* 339:1419–1423.
26. Lisiecki LE, Raymo ME (2005) A Pliocene-Pleistocene stack of 57 globally distributed benthic $\delta^{18}O$ records. *Paleoceanography* 20:PA1003.
27. Lang DC, et al. (2014) The transition on North America from the warm humid Pliocene to the glaciated Quaternary traced by eolian dust deposition at a benchmark North Atlantic Ocean drill site. *Quat Sci Rev* 93:125–141.
28. Ridgwell A (2003) Implications of the glacial $CO_2$ "iron hypothesis" for Quaternary climate change. *Geochem Geophys Geosyst* 4:1076.
29. Martínez-García A, et al. (2014) Iron fertilization of the Subantarctic ocean during the last ice age. *Science* 343:1347–1350.
30. Martin JH, Gordon RM, Fitzwater SE (1990) Iron in Antarctic waters. *Nature* 345: 156–158.
31. McGee D, Broecker WS, Winckler G (2010) Gustiness: The driver of glacial dustiness? *Quat Sci Rev* 29:2340–2350.
32. Kohfeld KE, Harrison SP (2001) DIRTMAP: The geological record of dust. *Earth Sci Rev* 54:81–114.
33. Myhre G, Highwood EJ, Shine KP, Stordal F (1998) New estimates of radiative forcing due to well mixed greenhouse gases. *Geophys Res Lett* 25:2715–2718.
34. Foster GL, Rae JWB (2016) Reconstructing ocean pH with boron isotopes in foraminifera. *Annu Rev Earth Planet Sci* 44:207–237.
35. Takahashi T, et al. (2009) Climatological mean and decadal change in surface ocean $pCO_2$, and net sea–air $CO_2$ flux over the global oceans. *Deep Sea Res Part II Top Stud Oceanogr* 56:554–577.
36. Henehan MJ, et al. (2013) Calibration of the boron isotope proxy in the planktonic foraminifera *Globigerinoides ruber* for use in palaeo-$CO_2$ reconstruction. *Earth Planet Sci Lett* 364:111–122.
37. Edgar KM, Anagnostou E, Pearson PN, Foster GL (2015) Assessing the impact of diagenesis on $\delta^{11}B$, $\delta^{13}C$, $\delta^{18}O$, Sr/Ca and B/Ca values in fossil planktic foraminiferal calcite. *Geochim Cosmochim Acta* 166:189–209.
38. Paillard D, Labeyrie L, Yiou P (1996) Analyseries 1.0: A Macintosh software for the analysis of geographical time-series. *Eos* 77:379.
39. Schmidt MW, Vautravers MJ, Spero HJ (2006) Western Caribbean sea surface temperatures during the late Quaternary. *Geochem Geophys Geosyst* 7:Q02P10.
40. Barker S, Greaves M, Elderfield H (2003) A study of cleaning procedures used for foraminiferal Mg/Ca paleothermometry. *Geochem Geophys Geosyst*, 10.1029/2003GC000559.
41. Yu JM, Elderfield H (2007) Benthic foraminiferal B/Ca ratios reflect deep water carbonate saturation state. *Earth Planet Sci Lett* 258:73–86.
42. Rae JW, Foster GL, Schmidt DN, Elliott T (2011) Boron isotopes and B/Ca in benthic foraminifera: Proxies for the deep ocean carbonate system. *Earth Planet Sci Lett* 302: 403–413.
43. Foster GL, et al. (2013) Interlaboratory comparison of boron isotope analyses of boric acid, seawater and marine $CaCO_3$ by MC-ICPMS and NTIMS. *Chem Geol* 358:1–14.
44. Evans D, Müller W (2012) Deep time foraminifera Mg/Ca paleothermometry: Nonlinear correction for secular change in seawater Mg/Ca. *Paleoceanography* 27: PA4205.
45. Fantle MS, DePaolo DJ (2006) Sr isotopes and pore fluid chemistry in carbonate sediment of the Ontong Java Plateau: Calcite recrystallization rates and evidence for a rapid rise in seawater Mg over the last 10 million years. *Geochim Cosmochim Acta* 70:3883–3904.
46. Delaney ML, Bé AWH, Boyle EA (1985) Li, Sr, Mg, and Na in foraminiferal calcite shells from laboratory culture, sediment traps, and sediment cores. *Geochim Cosmochim Acta* 49:1327–1341.
47. Klochko K, Kaufman AJ, Yao WS, Byrne RH, Tossell JA (2006) Experimental measurement of boron isotope fractionation in seawater. *Earth Planet Sci Lett* 248:276–285.
48. Catanzaro EJ (1970) *Boric Acid: Isotopic and Assay Standard Reference Materials* (US National Bureau of Standards, Gaithersburg, MD), Special Publication 260-17.
49. Hemming NG, Reeder RJ, Hanson GN (1995) Mineral-fluid partitioning and isotopic fractionation of boron in synthetic calcium carbonate. *Geochim Cosmochim Acta* 59: 371–379.
50. Hemming NG, Hanson GN (1992) Boron isotopic composition and concentration in modern marine carbonates. *Geochim Cosmochim Acta* 56:537–543.
51. Dickson AG (1990) Thermodynamics of the dissociation of boric acid in synthetic seawater from 273.15 to 318.15 K. *Deep Sea Res A Oceanogr Res Pap* 37:755–766.
52. Foster GL, von Strandmann P, Rae JWB (2010) Boron and magnesium isotopic composition of seawater. *Geochem Geophys Geosyst*, 10.1029/2010GC003201.
53. Foster GL, Lear CH, Rae JWB (2012) The evolution of $pCO_2$, ice volume and climate during the middle Miocene. *Earth Planet Sci Lett* 341–344:243–254.
54. Raitzsch M, Hönisch B (2013) Cenozoic boron isotope variations in benthic foraminifers. *Geology* 41:591–594.
55. Lemarchand D, Gaillardet J, Lewin E, Allegre C (2002) Boron isotope systematics in large rivers: Implications for the marine boron budget and paleo-pH reconstruction over the Cenozoic. *Chem Geol* 190:123–140.
56. Toggweiler J (1999) Variation of atmospheric $CO_2$ by ventilation of the ocean's deepest water. *Paleoceanography* 14:571–588.
57. Farrell JW, Prell WL (1991) Pacific $CaCO_3$ preservation and $\delta^{18}O$ since 4 Ma: Paleoceanic and paleoclimatic implications. *Paleoceanography* 6:485–498.
58. Catubig NR, et al. (1998) Global deep-sea burial rate of calcium carbonate during the Last Glacial Maximum. *Paleoceanography* 13:298–310.
59. R Development Core Team (2010) R: A language and environment for statistical computing (R Foundation for Statistical Computing, Vienna, Austria).
60. Gattuso J-P, et al. (2011) seacarb: Seawater carbonate chemistry with R. R package version 3.1.1. Available at https://cran.r-project.org/web/packages/seacarb/index.html.
61. York D, Evensen NM, Martínez ML, Delgado JDB, Derek Y (2004) Unified equations for the slope, intercept, and standard errors of the best straight line least-squares fitting of a straight line. *Am J Phys* 72:367–375.
62. De Boer B, Stocchi P, Van De Wal R (2014) A fully coupled 3-D ice-sheet-sea-level model: Algorithm and applications. *Geosci Model Dev* 7:2141–2156.
63. Archer D (1991) Modeling the calcite lysocline. *J Geophys Res Oceans* 96:17037–17050.
64. Sigman DM, McCorkle DC, Martin WR (1998) The calcite lysocline as a constraint on glacial/interglacial low-latitude production changes. *Global Biogeochem Cycles* 12: 409–427.
65. Robinson RS, et al. (2005) Diatom-bound $^{15}N/^{14}N$: New support for enhanced nutrient consumption in the ice age subantarctic. *Paleoceanography* 20:PA3003.

66. Franois R, et al. (1997) Contribution of Southern Ocean surface-water stratification to low atmospheric $CO_2$ concentrations during the last glacial period. *Nature* 389:929–935.
67. Robinson RS, Brunelle BG, Sigman DM (2004) Revisiting nutrient utilization in the glacial Antarctic: Evidence from a new method for diatom-bound N isotopic analysis. *Paleoceanography* 19:PA3001.
68. Studer AS, et al. (2015) Antarctic Zone nutrient conditions during the last two glacial cycles. *Paleoceanography* 30:845–862.
69. Duplessy J, et al. (1988) Deepwater source variations during the last climatic cycle and their impact on the global deepwater circulation. *Paleoceanography* 3:343–360.
70. Sarnthein M, et al. (1994) Changes in East Atlantic deepwater circulation over the last 30,000 years: Eight time slice reconstructions. *Paleoceanography* 9:209–267.
71. Sigman DM, Lehman SJ, Oppo DW (2003) Evaluating mechanisms of nutrient depletion and $^{13}C$ enrichment in the intermediate-depth Atlantic during the last ice age. *Paleoceanography* 18:1072.
72. Lynch-Stieglitz J, et al. (2007) Atlantic meridional overturning circulation during the last glacial maximum. *Science* 316:66–69.
73. Hain MP, Sigman DM, Haug GH (2014) *Treatise on Geochemistry* (Elsevier, Amsterdam), 2nd Ed, Vol 8, pp 485–517.
74. Pena LD, Goldstein SL (2014) Thermohaline circulation crisis and impacts during the mid-Pleistocene transition. *Science* 345:318–322.
75. Shipboard Scientific Party (1999) Leg 177 summary: Southern Ocean paleoceanography. *Proceedings of the Ocean Drilling Program, Initial Reports*, eds Gersonde R, et al. (Ocean Drilling Program, College Station, TX), Vol 177.
76. Powell MJ (1964) An efficient method for finding the minimum of a function of several variables without calculating derivatives. *Comput J* 7:155–162.
77. Brent RP (1973) Some efficient algorithms for solving systems of nonlinear equations. *SIAM J Numer Anal* 10:327–344.
78. Brent RP (2013) *Algorithms for Minimization Without Derivatives* (Prentice-Hall, Englewood Cliffs, NJ).
79. Fletcher R, Reeves CM (1964) Function minimization by conjugate gradients. *Comput J* 7:149–154.